

Ultrafast Hole Spin Qubit with Gate-Tunable Spin-Orbit Switch

F. N. M. Froning¹, L. C. Camenzind¹, O. A. H. van der Molen^{1,2}, A.

Li², E. P. A. M. Bakkers², D. M. Zumbühl¹, and F. R. Braakman¹

1: University of Basel, Klingelbergstrasse 82, 4056 Basel, Switzerland and

2: Department of Applied Physics, Eindhoven University of Technology,

P.O. Box 513, 5600 MB Eindhoven, The Netherlands

Abstract

A key challenge in quantum computation is the implementation of fast and local qubit control while simultaneously maintaining coherence [1]. Qubits based on hole spins offer, through their strong spin-orbit interaction, a way to implement fast quantum gates [2–5]. Strikingly, for hole spins in one-dimensional germanium and silicon devices, the spin-orbit interaction has been predicted to be exceptionally strong yet highly tunable with gate voltages. Such electrical control would make it possible to switch on demand between qubit idling and manipulation modes [6]. Here, we demonstrate ultrafast and universal quantum control of a hole spin qubit in a germanium/silicon core/shell nanowire [7, 8], with Rabi frequencies of several hundreds of megahertz, corresponding to spin-flipping times as short as ~ 1 ns - a new record for a single-spin qubit. Next, we show a large degree of electrical control over the Rabi frequency, Zeeman energy, and coherence time - thus implementing a switch toggling from a rapid qubit manipulation mode to a more coherent idling mode. We identify an exceptionally strong but gate-tunable spin-orbit interaction as the underlying mechanism, with a short associated spin-orbit length that can be tuned over a large range down to 3 nm for holes of heavy-hole mass. Our work demonstrates a spin-orbit qubit switch and establishes hole spin qubits defined in one-dimensional germanium/silicon nanostructures as a fast and highly tunable platform for quantum computation.

I. INTRODUCTION

Spin qubits defined in silicon (Si) and germanium (Ge) quantum dots are of particular interest for scaling up quantum circuits due to their small size, speed of operation, and compatibility with semiconductor industry [9–12]. Both materials feature a low natural abundance of non-zero nuclear spins, which has led to the demonstration of long qubit coherence times [9, 13, 14], as well as single- [14–16] and two-qubit [5, 17–19] operations with high fidelity. Most of this research has been performed using electron spin states defining the qubit [20]. Hole spin qubits [2, 12] have recently gained attention since they potentially enable faster quantum operations and a higher level of control over qubit parameters [3, 6, 21, 22]. In addition, hole spins in Ge and Si may have improved relaxation and decoherence times, since they do not exhibit a valley degeneracy and their wave function has reduced overlap with nuclear spins [23, 24]. Importantly, spin-orbit interaction (SOI) can be exceptionally strong for hole spins, particularly in Ge- or Si-based nanowires [3, 21]. This enables very fast spin control through electric-dipole spin resonance (EDSR) [25–28], where a time-varying electric field periodically displaces the hole wave function, thus creating an effective periodic magnetic field through the SOI. In this way, EDSR can be used for all-electrical spin manipulation without requiring micromagnets [29] or co-planar striplines [30], which add to device complexity.

Rabi frequencies of around 100 MHz have been measured for hole spins [4, 5], but predictions for one-dimensional systems range even up to 5 GHz, made possible by the particularly strong direct Rashba spin-orbit interaction (DRSOI) [6, 21]. Conversely, this strong SOI may lead to an undesired enhancement of qubit relaxation and dephasing rates, via coupling to phonons or charge noise. However, the DRSOI is also predicted to be tunable to a large extent through local electric fields [3, 21, 22], enabling electrical control over the SOI strength and Landé g -factor. Such electrical tunability provides a path towards a spin qubit with switchable interaction strength, using what we term a *spin-orbit switch*. The spin-orbit switch can be used to selectively idle a qubit in an isolated configuration of weak SOI and low decoherence (*OFF*-state), while for fast manipulation it is tuned to a regime of strong SOI (*ON*-state) and is selectively coupled to an EDSR driving field or microwave resonator by controlling the qubit Zeeman energy [6, 31]. Here, we experimentally realize the key components of this approach, through the demonstration of an ultrafast and electrically tunable

hole spin qubit in a Ge/Si core/shell nanowire. We use SOI-mediated EDSR to perform fast two-axis qubit control and implement Ramsey and Hahn echo pulsing techniques to compare the qubit’s coherence times. We then demonstrate a high degree of electrical control over the Rabi frequency, g -factor, and driven qubit decay time by tuning the voltage on one of the dot-defining gates, illustrating the basic ingredients of a spin-orbit switch. We extract a spin-orbit length that is extraordinarily short and electrically tunable. This control allows us to optimize our qubit for speed of operation, resulting in Rabi frequencies as large as 435 MHz.

II. SETUP AND MEASUREMENT TECHNIQUES

Figure 1 **a** shows a scanning electron micrograph of the device comprising five gates beneath a Ge/Si core/shell nanowire [8, 32, 33]. A depletion-mode few-hole double quantum dot (DQD) is formed inside the nanowire by positively biasing the five bottom gates. Throughout this work, we perform measurements of electronic transport through the DQD, using the source (S) and drain (D) contacts indicated in Figure 1 **a** (for more details about the device and measurement setup, see Methods). We operate the DQD at a transition exhibiting Pauli spin blockade [34], which we use for spin readout in transport measurements.

In our setup, gates L and LP are connected via bias-tees to high-frequency lines as indicated in Figure 1 **a**, allowing us to apply square voltage pulses and microwave bursts to these gates. The measurements are performed with a two-stage pulse scheme (see inset Fig. 1 **a**). First, the system is initialized at point I (see Fig. 1 **b**) in a spin-blockaded triplet state. Then, with a square pulse of depth ΔV_P , it is pulsed into Coulomb blockade to point M where a microwave burst of duration t_{burst} is applied. Finally, back at the readout point R, a current signal is measured if the spins were in a singlet configuration after manipulation.

Figures 1 **c** and **d** show typical EDSR measurements, where the microwave frequency f_{MW} is swept versus the applied magnetic field \vec{B}_{ext} along the \hat{x} - and \hat{y} -axis, respectively. On resonance, when \vec{B}_{ext} is perpendicular to the \hat{z} -axis, the spin is rotated, lifting spin blockade and leading to an increased current. From Figures 1 **c** and **d**, we extract $g_x = 1.06$ and $g_y = 1.02$. With \vec{B}_{ext} aligned along the \hat{z} direction, no EDSR signal could be observed, as will be discussed later.

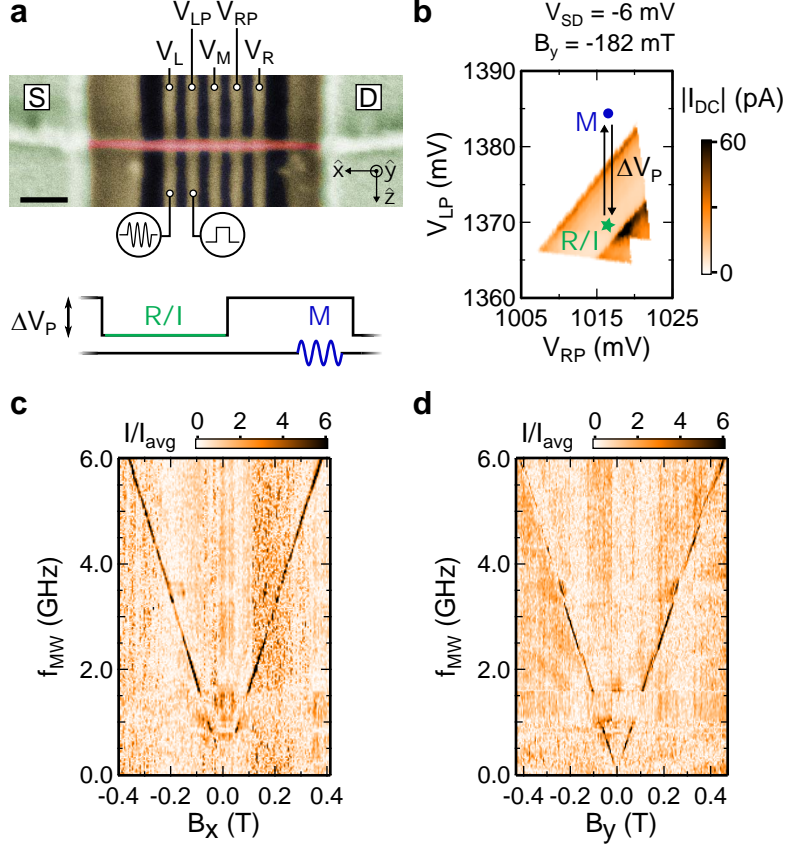


Figure 1. **Experimental setup and electric dipole spin resonance.** **a** Scanning electron micrograph of a cofabricated device, showing source (S) and drain (D) contacts and gates, as labeled. The scalebar corresponds to 100 nm. The inset at the bottom illustrates the pulse scheme. The points R, I and M indicate the locations of the readout, initialization, and manipulation stages, respectively, of the pulsing scheme (see **b**). The depth of the square pulse is ΔV_P . **b** Measurement of a set of bias triangles taken with a source-drain voltage $V_{SD} = -6$ mV showing Pauli spin blockade which is partially lifted at a finite magnetic field $B_y = -182$ mT. **c**, **d** Spin blockade leakage current indicating electric dipole spin resonance as a function of microwave frequency and magnetic field magnitude in \hat{x} (**c**) and \hat{y} (**d**) direction. For detailed measurement parameters, see Methods.

III. COHERENT MANIPULATION AND TWO-AXIS CONTROL

To demonstrate coherent control, we now vary the pulse duration t_{burst} and observe Rabi oscillations, in the form of the typical chevron pattern shown in Figure 2 **a**. Figure 2 **b** shows the dependence on the microwave power P_{MW} . From line cuts, we extract the Rabi

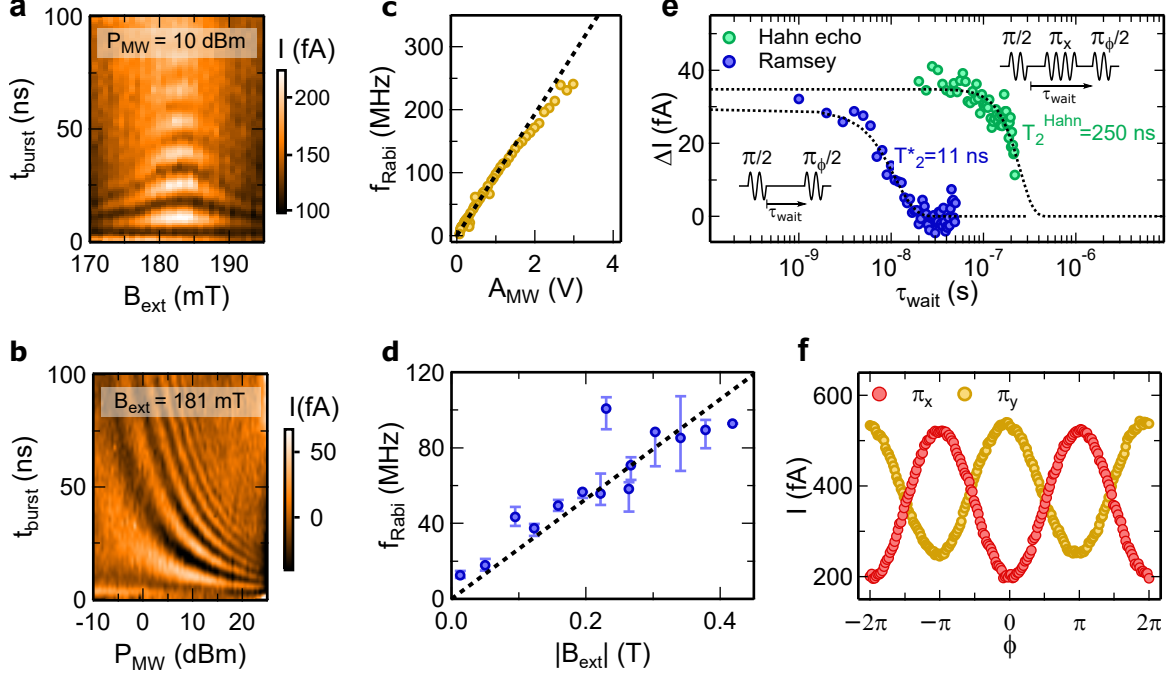


Figure 2. **Coherent qubit control.** **a** Measurement of the current as a function of microwave burst duration and magnetic field. We observe a Rabi frequency of 72 MHz. **b** Power dependence of Rabi oscillations in the same configuration as in **a**. **c** Extracted Rabi frequency as a function of the microwave amplitude, from fits of the data in **b** (see Methods for details). The black dashed line is a linear fit to the extracted Rabi frequencies. **d** Rabi frequency as a function of the magnitude of the external magnetic field. The black dashed line is a linear fit to the data over the whole range with zero offset. **e** Decay of Ramsey fringes (blue points) and Hahn echo (green points) as a function of the waiting time τ_{wait} between the two $\frac{\pi}{2}$ -pulses. Insets show pulse sequences used for Ramsey (bottom left) and Hahn echo (top right). Black dotted lines are fits of the data to exponential decay. **f** Demonstration of two-axis qubit control by applying a Hahn echo sequence with two orthogonal π pulses. The amplitudes of the fringes of the two datasets differ due to an offset in the calibration of the $\frac{\pi}{2}$ -pulse duration between the two measurements.

frequency f_{Rabi} (see Methods), which is shown in Figure 2 **c** as a function of the microwave amplitude. The data at low amplitudes is in good agreement with a linear fit (black dashed line in Fig. 2**c**), as expected theoretically. The saturation behaviour at higher amplitudes is likely due to anharmonicity in dot confinement for the particular gate voltage configuration used here.

In the presence of SOI, the oscillating electric field on gate V_{LP} due to the microwaves gives rise to an oscillating effective magnetic field $\vec{B}_{\text{eff}}(t)$, with magnitude [25]:

$$|\vec{B}_{\text{eff}}(t)| = 2|\vec{B}_{\text{ext}}| \cdot \frac{l_{\text{dot}}}{l_{\text{so}}} \cdot \frac{e|\vec{E}_{\text{MW}}(t)|l_{\text{dot}}}{\Delta_{\text{orb}}}, \quad (1)$$

with e the elementary charge, $\vec{E}_{\text{MW}}(t)$ the ac electric field in the dot generated by the microwaves, l_{dot} the dot length, $\Delta_{\text{orb}} \propto l_{\text{dot}}^{-2} m_{\text{eff}}^{-1}$ the orbital level splitting, and l_{so} the spin-orbit length, defined here as the distance a hole has to travel along the nanowire to have its spin flipped due to SOI. This effective field \vec{B}_{eff} drives the Rabi oscillations, with Rabi frequency $f_{\text{Rabi}} = g_{\perp} \mu_{\text{B}} |\vec{B}_{\text{eff}}(t)| / 2h$, with g_{\perp} the g -factor along the direction of \vec{B}_{eff} and thus perpendicular to \vec{B}_{ext} . From equation (1) we see that $|\vec{B}_{\text{eff}}|$ scales linearly with $|\vec{B}_{\text{ext}}|$. We measure the Rabi frequency for different $|\vec{B}_{\text{ext}}|$ and plot the result in Figure 2 d. Here, the error bars reflect the inaccuracy of the frequency-dependent microwave power calibration (see Section 1 of the Supplementary Information). Nevertheless, the measurement agrees well with a linear dependence of the Rabi frequency on $|\vec{B}_{\text{ext}}|$, as expected for SOI-mediated EDSR [25, 26].

Next, in order to characterize the free induction decay, we apply a Ramsey pulse sequence, as depicted in Figure 2 e. A fit to a Gaussian decay yields the dephasing time $T_2^* = 11(1)$ ns. This value is one order of magnitude smaller than in comparable hole spin qubit systems [4, 5, 35]. This may be attributed to low-frequency noise, which could for instance be due to gate voltage fluctuations, frequency jitter of the microwave source, charge fluctuators, or residual nuclear spin noise. Nevertheless, we can mitigate this to a large extent using a Hahn echo sequence, prolonging coherence by a factor of ~ 25 , thus demonstrating efficient decoupling of the qubit from low-frequency noise.

Finally, we use a modified Hahn echo pulse sequence to demonstrate two-axis control. We employ either a π_x - or a π_y -pulse and vary the phase of the second $\pi_{\phi}/2$ -pulse (see schematics in Fig. 2 e). This results in two sets of Ramsey fringes as shown in Figure 2 f, which are phase-shifted by π . These measurements demonstrate universal, two-axis control of the hole spin qubit.

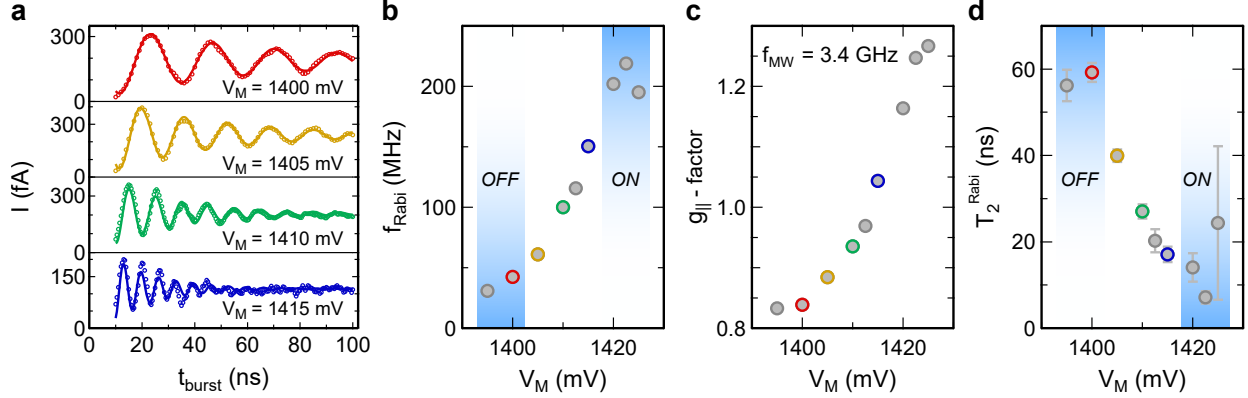


Figure 3. **Electrical tunability of qubit parameters.** **a** Rabi oscillations for four different gate voltage values V_M . Here, all parameters were kept constant, except when indicated in the plots. **b**, **c**, **d** Rabi frequency, g -factor, and T_2^{Rabi} as a function of the gate voltage V_M , as extracted from fits to line cuts such as shown in **a**. Insets in **b** and **d** indicate possible idling (*OFF*) and manipulation (*ON*) points.

IV. SPIN-ORBIT SWITCH AND ANISOTROPY

The measurements of Figure 2 establish Ge/Si nanowires as a platform for hole spin qubits. Remarkably, the particular DRSOI [3, 21] provides a unique way to electrically control the qubit via the SOI strength and qubit Zeeman energy [6, 22]. This tunability can be exploited for optimizing qubit relaxation and dephasing times, as well as selective coupling of the qubit to EDSR drive fields or microwave resonators [6, 36, 37]. Here, we demonstrate this distinct gate-tunability of hole spin qubits in Ge/Si core/shell nanowires, where we investigate electrical control over the g -factor, Rabi frequency, and coherence time.

The gate voltages not only provide the electrostatic confinement but also constitute a static electric field on the order of tens of $\text{V}/\mu\text{m}$ inside the quantum dots, which has a significant effect on the strength of SOI [3, 21]. Figure 3 **a** shows example Rabi oscillations for four different gate voltages V_M . Here, f_{MW} and P_{MW} are kept fixed, while $|\vec{B}_{\text{ext}}|$ is adjusted to compensate for changes in the g_{\parallel} -factor along B_{ext} , keeping the qubit on resonance with the microwave drive. As shown in Figure 3 **b**, we find that the Rabi frequency depends strongly on V_M , with a gate voltage change of 30 mV resulting in a 7-fold increase of the Rabi frequency.

For SOI-mediated spin rotations [25], the Rabi frequency is proportional to the effective

magnetic field given by Eq. (1) and the g -factor g_{\perp} . Therefore, the Rabi frequency depends on the spin-orbit length l_{so} , the ac electric field $|\vec{E}_{\text{MW}}(t)|$ created through the periodic gate voltage modulation, \vec{B}_{ext} , the quantum dot confinement Δ_{orb} , and the g -factor. Despite an observed change of g_{\parallel} with V_{M} [22, 38] by a factor of 1.5 (see Fig. 3 c), the effect on the Rabi frequency is small: at constant Zeeman energy, we can write $f_{\text{Rabi}} \propto f_{\text{MW}} \cdot g_{\perp}/g_{\parallel}$. Hence, if the g -factor anisotropy g_{\perp}/g_{\parallel} is only weakly affected by gate voltages, as observed here (see Supplementary Information Figs. S3 d, e), then the Rabi frequency change is correspondingly small.

We have carefully analyzed each of the contributions to the change of the Rabi frequency (see Section 2.2 of the Supplementary Information) and find that the large change must mostly be attributed to a gate-tunability of the spin-orbit length l_{so} . Using equation (1), we extract upper bounds of l_{so} (see Supplementary Information Section 2.2.1). We find remarkably short values of l_{so} that are tuned from 28 nm down to 3 nm. Here we assume a heavy-hole effective mass, as suggested by independent transport measurements at high magnetic field [39]. Such a strong SOI was predicted for the DRSOI [3, 21]. This range of l_{so} overlaps with values found in antilocalization [40] and spin blockade experiments [39].

Besides the Rabi frequency, also the coherence is strongly affected by V_{M} , as shown in Figure 3 a. We plot the characteristic driven decay time T_2^{Rabi} in Figure 3 d, finding that it scales roughly inversely with f_{Rabi} and g_{\parallel} : a short decay time coincides with a high Rabi frequency, and vice versa. Together with the tunability of the Rabi frequency, this control over the qubit coherence time allows us to define (see insets Figs. 3 b and d) a fast qubit manipulation point (*ON*) and a qubit idling point featuring significantly improved coherence (*OFF*), demonstrating the full functionality of the spin-orbit switch.

Moreover, the variation of g_{\parallel} in Figure 3 c effectively adds a third mode of operation to the spin-orbit switch, where individual qubits can be selectively tuned, for instance in and out of resonance with a microwave cavity, enabling a switch for qubit-resonator coupling [36, 37]. Finally, we find that the pulse depth ΔV_{P} can also be used to tune f_{Rabi} and g_{\parallel} (see Section 2.1 of the Supplementary Information), indicating that dynamically pulsing these quantities is feasible.

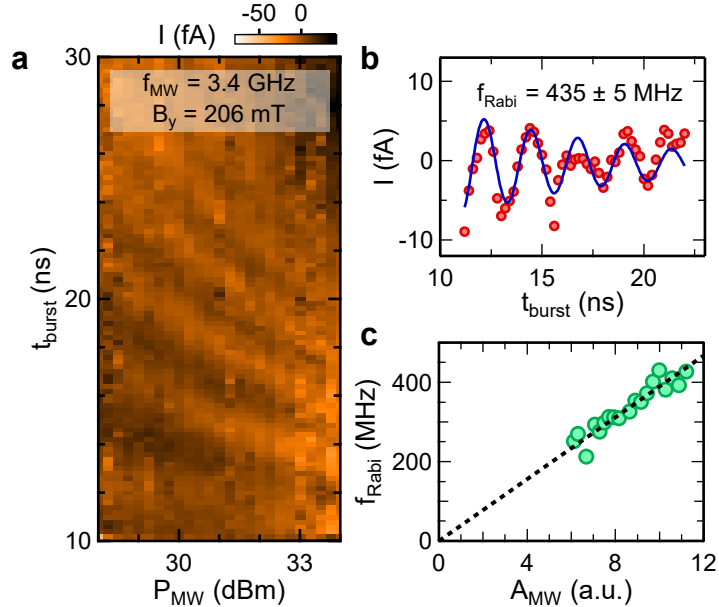


Figure 4. **Ultrafast coherent control.** **a** Power-dependence of ultrafast Rabi oscillations. **b** Line cut of data shown in **a** at a microwave power of 34 dBm. The data is fitted (blue solid curve) as in Fig. 2, after subtraction of a linear background. **c** Rabi frequency as a function of microwave amplitude, extracted from fits to line cuts in **a**.

V. ULTRAFAST RABI OSCILLATIONS

In a next step, we now use the electrical tunability to optimize the gate voltages for a high Rabi frequency and furthermore increase the applied microwave power. In Figure 4, we show a measurement of ultrafast Rabi oscillations, with the maximum Rabi frequency reaching a value of $435(5)$ MHz (see Fig. 4 **b**), allowing for spin-flip times of the qubit as short as 1.15 ns. As can be seen in Figure 4 **c**, the Rabi frequency scales linearly with applied microwave amplitude in this regime of ultrafast qubit operation and shows no signs of saturation for the gate configuration used here, in contrast to Figure 2 **b**. This indicates that even higher Rabi frequencies may be possible through the application of a higher microwave power. Note that pulse imperfections play a larger role for shorter pulse duration and higher amplitudes, which likely partially explains the decrease in T_2^{Rabi} with increased microwave amplitude.

Remarkably, the observed Rabi frequencies of over 400 MHz are roughly $\frac{1}{8}$ of the Larmor precession frequency of 3.4 GHz. The system is thus approaching the strong driving regime where the rotating wave approximation is not applicable anymore, opening the possibility

for ultrafast, non-sinusoidal spin-flipping [41, 42] that has not been realized before with conventional spin qubits. We note that in our experiment, effects of strong driving [42] could contribute to the reduced visibility of Rabi oscillations at the high Rabi frequencies shown in the measurements of Figure 4.

VI. CONCLUSIONS AND OUTLOOK

In summary, we have demonstrated ultrafast two-axis control via EDSR of a hole spin qubit in a Ge/Si core/shell nanowire. Our measurements firmly demonstrate the feasibility of single-spin qubit operations on nanosecond timescales. Ideally, such fast operations would be combined with long qubit coherence times. Although we observe a relatively short inhomogeneous dephasing time, we measure a much larger spin echo decay time, which indicates the presence of low-frequency noise affecting our qubit. The use of a charge sensor will allow to decouple the quantum dots from the neighboring Fermi reservoirs, likely leading to a significant further enhancement of the coherence time.

We have demonstrated a remarkable 7-fold increase of the Rabi frequency for a relatively small change in gate voltage. Similarly, we find that the driven decay time of our qubit can be tuned by the same gate voltage, demonstrating the basic workings of the spin-orbit switch. Our measurements indicate the presence of an exceptionally strong spin-orbit interaction in Ge/Si core/shell nanowires, in qualitative agreement with predictions of DRSOI [3, 21]. A more quantitative comparison to theory, as well as improved gate switching, requires precise engineering of the electric field and single-hole dot occupation, both of which can be achieved through optimization of the gate design.

The high tunability of the qubit demonstrates the suitability of the platform for the implementation of a qubit with switchable interaction strengths. The effect of the gate voltages and the pulse depth on the qubit resonance frequency and the Rabi frequency have the potential to dynamically pulse the characteristic qubit parameters and interaction strengths from a qubit manipulation to an idling point. Furthermore, the spin-orbit switch could allow tuning to ‘sweet spots’ of operation, where the SOI strength is to first order insensitive to charge noise, leading to enhancement of qubit coherence [3]. Finally, the

strong spin-orbit interaction holds great potential for realizing fast entangling operations between distant spin qubits, mediated by a microwave resonator [6, 31, 36, 37, 43].

VII. METHODS

A. Device Fabrication

The device features a set of five gates with a width of 20 nm and a pitch of 50 nm defined by electron beam lithography (EBL) on a p^{++} -doped Si chip covered with 290 nm of thermal oxide. The gates are covered by a 20 nm thick layer of Al_2O_3 grown by atomic layer deposition in order to electrically insulate them from the nanowire. A single Ge/Si core/shell nanowire with a core radius of about 10 nm and a shell thickness of 2.5 nm [8] is placed deterministically across the set of gates using a micromanipulator. The nanowire is roughly aligned with the coordinate system in Figure 1 b but the exact angle in the $\hat{x}\hat{z}$ plane is unknown. Finally, ohmic contacts are fabricated by EBL and metallized with Ti/Pd following a short dip in hydrofluic acid to remove the native oxide. The scanning electron micrograph shown in Fig. 1 a is from a similarly fabricated device as used here.

B. Experimental Setup

The sample is wire-bonded to a printed-circuit board (PCB) providing dc wiring and RF lines, coupled via bias tees. The PCB is mounted in a Bluefors dilution refrigerator with a base temperature around $T_{\text{base}} = 10$ mK, at which temperature all measurements are taken. Each high-frequency line includes attenuators with combined values of ~ 30 dB. A Basel Precision Instruments LNHR DAC is used to supply the dc voltages, and a Basel Precision Instruments LNHS I/V converter is used for readout of the qubit in transport.

A Tektronix 7122C or AWG5208 arbitrary waveform generator (AWG) is used to generate the square voltage pulses applied to gate V_{LP} . To drive the qubit, either an analog Keysight E8257D signal generator or a E8267D vector signal generator supplies the microwave tone. For measurements at high microwave power a RF-Lambda model RFQ132070 amplifier was used. Two different configurations of the setup are used for microwave burst generation. For the measurements in Figures 1 c-d, 2 d, 3, and 4, the amplitude of the microwaves is modulated by means of an RF-switch (ZASWA-2-50DRA+ from MiniCircuits), triggered

by the AWG. The RF-switch has a minimum pulse width of 10 ns. For the measurements in Figures 1 b, 2 a-c, e, f, the microwave bursts are generated by IQ modulation of the vector signal generator’s microwave tone. Here, the minimum pulse width is 6 ns. In either configuration, a lock-in amplifier is used to chop the bursted microwaves at a frequency of 89.75 Hz and the I/V converter output is demodulated at his frequency. This allows us to separate the current signal due to the applied microwaves from the background.

C. Data Analysis

Rabi frequencies are extracted from fits to $I(t_{\text{burst}}) = I_0 + C \cdot \sin(2\pi f_{\text{Rabi}} t_{\text{burst}} + \phi) \cdot \exp(-t_{\text{burst}}/T_2^{\text{Rabi}})$. Here, I_0 is an offset, C the amplitude, ϕ a phase shift, and T_2^{Rabi} the characteristic decay time. Furthermore, we post-processed raw data sets in the following ways. The data in Fig. 1 c (1 d) was offset by 10 mT (20 mT) to compensate for trapped magnetic flux. Furthermore, the average value has been subtracted from each column and row of the raw data. Then each row has been divided by the average row value. Similarly, for the plots of Fig. 2 b and 4 a, the average value has been subtracted from each column and row of the raw data. In Fig. 4 a, data for microwave burst times below the minimum pulse width achievable by our electronics is omitted.

D. Measurement Details

In the following we list the relevant parameters that were used for the various measurements. For the measurements of Figs. 1 c-d, a fixed pulse amplitude $\Delta V_P = 0.55$ V and a burst duration $t_{\text{burst}} = 15$ ns was used. In Figs. 2 a-c, \vec{B}_{ext} was oriented along the $-\hat{y}$ -axis. For Fig. 2 d, $f_{\text{MW}} = 3.4$ GHz was used and \vec{B}_{ext} was oriented in the $\hat{x}\hat{y}$ -plane, making an angle of 40° with the \hat{y} -axis. In Fig. 2 e, the duration of the π -pulse $t_\pi = 13$ ns, $P_{\text{MW}} = 3$ dBm, $f_{\text{MW}} = 2.6$ GHz, and $|\vec{B}_{\text{ext}}| = 181$ mT along the $-\hat{x}$ -axis. For Fig. 2 f, we used $P_{\text{MW}} = 14$ dBm, $f_{\text{MW}} = 3.4$ GHz and $|\vec{B}_{\text{ext}}| = 292$ mT, along the same direction as used for Fig. 2 d. Finally, for the measurements of Fig. 3, we used $P_{\text{MW}} = 25$ dBm and the orientation of $|\vec{B}_{\text{ext}}|$ was the same as in Fig. 2 d.

For completeness, we also mention the other gate voltages used for the measurements of Fig. 3: $V_L = 3710$ mV and $V_R = 1495$ mV, V_{LP} and V_{RP} depend on V_M , but are similar to

the values used for Fig. 1 b.

ACKNOWLEDGMENTS

We thank Stefano Bosco, Bence Hetényi, Christoph Kloeffer, Daniel Loss, Arne Laucht, and Alex Hamilton for useful discussions. Furthermore, we acknowledge Sascha Martin and Michael Steinacher for technical support. This work was partially supported by the Swiss Nanoscience Institute (SNI), the NCCR QSIT, the Georg H. Endress Foundation, Swiss NSF (grant nr. 179024), the EU H2020 European Microkelvin Platform EMP (grant nr. 824109), and FET TOPSQUAD (grant nr. 862046).

-
- [1] M. A. Nielsen and I. Chuang, *Quantum Computation and Quantum Information*, 10th ed. (Cambridge University Press, New York, New York, 2010).
 - [2] D. V. Bulaev and D. Loss, [Phys. Rev. Lett. **95**, 076805 \(2005\)](#).
 - [3] C. Kloeffer, M. J. Rančić, and D. Loss, [Phys. Rev. B **97**, 235422 \(2018\)](#).
 - [4] H. Watzinger, J. Kukučka, L. Vukušić, F. Gao, T. Wang, F. Schäffler, J.-J. Zhang, and G. Katsaros, [Nat. Commun. **9**, 3902 \(2018\)](#).
 - [5] N. W. Hendrickx, D. P. Franke, A. Sammak, G. Scappucci, and M. Veldhorst, [Nature **577**, 487 \(2020\)](#).
 - [6] C. Kloeffer, M. Trif, P. Stano, and D. Loss, [Phys. Rev. B **88**, 241405 \(2013\)](#).
 - [7] W. Lu, J. Xiang, B. P. Timko, Y. Wu, and C. M. Lieber, [Proc. Natl. Acad. Sci. **102**, 10046 \(2005\)](#).
 - [8] S. Conesa-Boj, A. Li, S. Koelling, M. Brauns, J. Ridderbos, T. T. Nguyen, M. A. Verheijen, P. M. Koenraad, F. A. Zwanenburg, and E. P. A. M. Bakkers, [Nano Lett. **17**, 2259 \(2017\)](#).
 - [9] F. A. Zwanenburg, A. S. Dzurak, A. Morello, M. Y. Simmons, L. C. L. Hollenberg, G. Klimeck, S. Rogge, S. N. Coppersmith, and M. A. Eriksson, [Rev. Mod. Phys. **85**, 961 \(2013\)](#).
 - [10] C. Kloeffer and D. Loss, [Annu. Rev. Condens. Matter Phys. **4**, 51 \(2013\)](#).
 - [11] L. M. K. Vandersypen, H. Bluhm, J. S. Clarke, A. S. Dzurak, R. Ishihara, A. Morello, D. J. Reilly, L. R. Schreiber, and M. Veldhorst, [Npj Quantum Inf. **3**, 34 \(2017\)](#).

- [12] G. Scappucci, C. Kloeffer, F. A. Zwanenburg, D. Loss, M. Myronov, J.-J. Zhang, S. De Franceschi, G. Katsaros, and M. Veldhorst, [arXiv:2004.08133](#) (2020).
- [13] A. M. Tyryshkin, S. Tojo, J. J. L. Morton, H. Riemann, N. V. Abrosimov, P. Becker, H.-J. Pohl, T. Schenkel, M. L. W. Thewalt, K. M. Itoh, and S. A. Lyon, *Nat. Mater.* **11**, 143 (2012).
- [14] J. Yoneda, K. Takeda, T. Otsuka, T. Nakajima, M. R. Delbecq, G. Allison, T. Honda, T. Kodera, S. Oda, Y. Hoshi, N. Usami, K. M. Itoh, and S. Tarucha, *Nat. Nanotechnol.* **13**, 102 (2018).
- [15] E. Kawakami, P. Scarlino, D. R. Ward, F. R. Braakman, D. E. Savage, M. G. Lagally, M. Friesen, S. N. Coppersmith, M. A. Eriksson, and L. M. K. Vandersypen, *Nat. Nanotechnol.* **9**, 666 (2014).
- [16] M. Veldhorst, J. C. Hwang, C. H. Yang, A. W. Leenstra, B. De Ronde, J. P. Dehollain, J. T. Muhonen, F. E. Hudson, K. M. Itoh, A. Morello, and A. S. Dzurak, *Nat. Nanotechnol.* **9**, 981 (2014).
- [17] M. Veldhorst, C. H. Yang, J. C. C. Hwang, W. Huang, J. P. Dehollain, J. T. Muhonen, S. Simmons, A. Laucht, F. E. Hudson, K. M. Itoh, A. Morello, and A. S. Dzurak, *Nature* **526**, 410 (2015).
- [18] D. M. Zajac, A. J. Sigillito, M. Russ, F. Borjans, J. M. Taylor, G. Burkard, and J. R. Petta, *Science* **359**, 439 (2018).
- [19] T. F. Watson, S. G. J. Philips, E. Kawakami, D. R. Ward, P. Scarlino, M. Veldhorst, D. E. Savage, M. G. Lagally, M. Friesen, S. N. Coppersmith, M. A. Eriksson, and L. M. K. Vandersypen, *Nature* **555**, 633 (2018).
- [20] D. Loss and D. P. DiVincenzo, *Phys. Rev. A* **57**, 120 (1998).
- [21] C. Kloeffer, M. Trif, and D. Loss, *Phys. Rev. B* **84**, 195314 (2011).
- [22] F. Maier, C. Kloeffer, and D. Loss, *Phys. Rev. B* **87**, 161305 (2013).
- [23] C. H. Yang, A. Rossi, R. Ruskov, N. S. Lai, F. A. Mohiyaddin, S. Lee, C. Tahan, G. Klimeck, A. Morello, and A. S. Dzurak, *Nat. Commun.* **4**, 2069 (2013).
- [24] J. H. Prechtel, A. V. Kuhlmann, J. Houel, A. Ludwig, S. R. Valentin, A. D. Wieck, and R. J. Warburton, *Nat. Mater.* **15**, 981 (2016).
- [25] V. N. Golovach, M. Borhani, and D. Loss, *Phys. Rev. B* **74**, 165319 (2006).

- [26] K. C. Nowack, F. H. L. Koppens, Y. V. Nazarov, and L. M. K. Vandersypen, [Science](#) **318**, 1430 (2007).
- [27] D. V. Bulaev and D. Loss, [Phys. Rev. Lett.](#) **98**, 097202 (2007).
- [28] J. W. G. van den Berg, S. Nadj-Perge, V. S. Pribiag, S. R. Plissard, E. P. A. M. Bakkers, S. M. Frolov, and L. P. Kouwenhoven, [Phys. Rev. Lett.](#) **110**, 066806 (2013).
- [29] M. Pioro-Ladrière, T. Obata, Y. Tokura, Y.-S. Shin, T. Kubo, K. Yoshida, T. Taniyama, and S. Tarucha, [Nat. Phys.](#) **4**, 776 (2008).
- [30] F. H. L. Koppens, C. Buizert, K. J. Tielrooij, I. T. Vink, K. C. Nowack, T. Meunier, L. P. Kouwenhoven, and L. M. K. Vandersypen, [Nature](#) **442**, 766 (2006).
- [31] G. Burkard, M. J. Gullans, X. Mi, and J. R. Petta, [Nat. Rev. Phys.](#) **2**, 129 (2020).
- [32] F. N. M. Froning, M. K. Rehmann, J. Ridderbos, M. Brauns, F. A. Zwanenburg, A. Li, E. P. A. M. Bakkers, D. M. Zumbühl, and F. R. Braakman, [Appl. Phys. Lett.](#) **113**, 073102 (2018).
- [33] M. Brauns, J. Ridderbos, A. Li, W. G. van der Wiel, E. P. A. M. Bakkers, and F. A. Zwanenburg, [Appl. Phys. Lett.](#) **109**, 143113 (2016).
- [34] K. Ono, D. G. Austing, Y. Tokura, and S. Tarucha, [Science](#) **297**, 1313 (2002).
- [35] A. P. Higginbotham, T. W. Larsen, J. Yao, H. Yan, C. M. Lieber, C. M. Marcus, and F. Kuemmeth, [Nano Lett.](#) **14**, 3582 (2014).
- [36] M. Trif, V. N. Golovach, and D. Loss, [Phys. Rev. B](#) **77**, 045434 (2008).
- [37] S. E. Nigg, A. Fuhrer, and D. Loss, [Phys. Rev. Lett.](#) **118**, 147701 (2017).
- [38] O. Dmytruk, D. Chevallier, D. Loss, and J. Klinovaja, [Phys. Rev. B](#) **98**, 165403 (2018).
- [39] F. N. M. Froning, M. J. Rančić, B. Hetényi, S. Bosco, M. K. Rehmann, A. Li, E. P. A. M. Bakkers, F. A. Zwanenburg, D. Loss, D. M. Zumbühl, and F. R. Braakman, in preparation (2020).
- [40] A. P. Higginbotham, F. Kuemmeth, T. W. Larsen, M. Fitzpatrick, J. Yao, H. Yan, C. M. Lieber, and C. M. Marcus, [Phys. Rev. Lett.](#) **112**, 216806 (2014).
- [41] Y. Kato, R. C. Myers, D. C. Driscoll, A. C. Gossard, J. Levy, and D. D. Awschalom, [Science](#) **299**, 1201 (2003).
- [42] A. Laucht, S. Simmons, R. Kalra, G. Tosi, J. P. Dehollain, J. T. Muhonen, S. Freer, F. E. Hudson, K. M. Itoh, D. N. Jamieson, J. C. McCallum, A. S. Dzurak, and A. Morello, [Phys. Rev. B](#) **94**, 1 (2016).
- [43] F. Borjans, X. G. Croot, X. Mi, M. J. Gullans, and J. R. Petta, [Nature](#) **577**, 195 (2020).